Journal of Alloys and Compounds 842 (2020) 155859

Contents lists available at ScienceDirect

Journal of Alloys and Compounds

journal homepage: http://www.elsevier.com/locate/jalcom

Influence of rare-earth doping on the structural and dielectric properties of orthoferrite $La_{0.50}R_{0.50}FeO_3$ ceramics synthesized under high pressure

I.I. Makoed [a, b, *], N.A. Liedienov [a, c, **], A.V. Pashchenko [a, c], G.G. Levchenko [a, c], D.D. Tatarchuk [d], Y.V. Didenko [d], A.A. Amirov [e, f], G.S. Rimski [g], K.I. Yanushkevich [g]

[a] *State Key Laboratory of Superhard Materials, International Centre of Future Science of Jilin University, 130012, Changchun, China*
[b] *A.S. Pushkin Brest State University, 224016, Brest, Belarus*
[c] *Donetsk Institute for Physics and Engineering named after O.O. Galkin, NASU, 03028, Kyiv, Ukraine*
[d] *National Technical University of Ukraine "Igor Sikorsky KPI", 03056, Kyiv, Ukraine*
[e] *Institute of Physics, Dagestan Scientific Center of Russian Academy of Sciences, 367003, Makhachkala, Russia*
[f] *Laboratory of Novel Magnetic Materials & Institute of Physics Mathematics and Informational Technologies, Immanuel Kant Baltic Federal University, 236029, Kaliningrad, Russia*
[g] *Scientific-Practical Materials Research Center, NASB, 220072, Minsk, Belarus*

ARTICLE INFO

Article history:
Received 28 April 2020
Received in revised form
27 May 2020
Accepted 29 May 2020
Available online 9 June 2020

Keywords:
Orthoferrite
High pressure sintering
Rietveld method
Morphology
Colossal dielectric constant
Electrical module

ABSTRACT

The effect of co-doping on the structural and dielectric properties of the $La_{0.50}R_{0.50}FeO_3$ orthoferrites for a full number of substitutions (R = Ce–Lu) has been experimentally and theoretically studied using X-ray diffraction, SEM, EDS, and dielectric spectroscopy methods. The $La_{0.50}R_{0.50}FeO_3$ ceramics with R = Nd, Sm, Gd, Dy, and Er, prepared by a solid-state reaction method under cold pressing at high pressure $P = 4$ GPa, have been taken as a basis. Structural parameters in the $La_{0.50}R_{0.50}FeO_3$ orthoferrites have been obtained using Rietveld refinement of X-ray experimental data with their further approximation by linear dependence. Monotonic change in crystal lattice parameters, orthorhombic distortion degree, global instability index, and Goldschmidt tolerance factor have been observed for all samples doped by different R-cations. With increase in the radius of R-cation, a growth in an average grain size has been detected. The investigation of dielectric properties in a wide frequency range of 10^{-1}–10^{10} Hz and their theoretical description with determining main mechanisms of dielectric polarization made it possible to establish regularities among a type of doping R-cation, crystal-chemical parameters and dielectric properties. The studied ceramic $La_{0.50}R_{0.50}FeO_3$ samples demonstrate colossal dielectric constant ~ 10^4 and relatively small dielectric loss tangent in a low-frequency range. The obtained results can be useful for further application of orthoferrite-based materials as sensor and switching devices.

1. Introduction

Orthoferrites of $RFeO_3$, where R is rare-earth (RE) cation, have been the objects of scientific research for a long time due to the presence of unique physical properties [1–4]. These materials have found practical application as components of solid fuel elements [5], gas sensors [6], catalytic converters [7], and high-speed switches [8]. The presence of multiferroic properties in the orthoferrites has been detected recently [5,9], where the electric and magnetic ordered structures coexist. This makes it possible to create multifunctional elements of electronic circuits based on them. Promising materials for obtaining multiferroic properties are double orthoferrites of $R1_{1-x}R2_xFeO_3$ ($0 < x < 0.5$; $R1$, $R2$ = La–Lu), which simultaneously include two types of cations in a RE sublattice. The equal oxidation states of La^{3+} and R^{3+} during cation substitution do not cause a change in valence, which ensures the fulfillment of the electroneutrality condition in the obtained compositions. Smaller ions of R^{3+} with respect to the ionic radius of La^{3+} increase the distortion of the crystal lattice, which leads to a change in the structurally sensitive physical properties of the compositions. Now, a relatively small number of papers are known,

---

* Corresponding author. State Key Laboratory of Superhard Materials, International Centre of Future Science of Jilin University, 130012, Changchun, China.
** Corresponding author. State Key Laboratory of Superhard Materials, International Centre of Future Science of Jilin University, 130012, Changchun, China.
E-mail addresses: igmak2010@yandex.by (I.I. Makoed), nikita.ledenev.ssp@gmail.com (N.A. Liedienov).

https://doi.org/10.1016/j.jallcom.2020.155859

where structure and physical properties are studied in $LaFeO_3$ materials doped by different cations of Ce [5], Pr [10], Nd [11,12], Sm [11–13], Eu [14], Gd [12,15], Tb [16], Dy [17], Ho [18], Er [19], and Lu [20,21]. However, there is no data about simultaneous studying of structural and dielectric properties of $R1_{1\text{-}x}R2_xFeO_3$ orthoferrites for a full number of substitutions from La to Lu prepared at the same chemical conditions. In addition, the reasons for observation of the wide variety of physical properties in double orthoferrites are both the use of different preparation methods and variability of their synthesis conditions.

Thus, in this work, experimental and theoretical investigations of the mutual influence of various RE cations on the structural, microstructural and dielectric properties of the orthoferrite $La_{0.5}R_{0.5}FeO_3$ ceramics obtained by cold pressing at high pressure (4 GPa) have been discussed comprehensively.

2. Experimental section

The polycrystalline $La_{0.5}R_{0.5}FeO_3$ samples were synthesized by a solid-state reaction route [22]. The initial R_2O_3 (R = La (purity ≥ 99.5%); Er, Dy, Gd, Sm, and Nd (≥ 99.9%)), and Fe_2O_3 (≥ 99.5%) powders (Sigma Aldrich Chemicals) were mixed in a dried agate mortar for 5 h and then with ethanol for 2 h. The obtained mixture was preliminary synthesized at a temperature of 850 ± 50 °C in a ceramic vessel in air for 5 h. The heating rate was 10 K/min. After grinding and repeated synthesizing under the same conditions, X-ray diffraction studies of the obtained mixture for controlling the phase composition were carried out, afterwards the samples were finally synthesized under cold pressing at high pressure $P = 4.00 \pm 0.04$ GPa for a short time of 1 min [23]. Creation of working pressure from atmospheric to 4 GPa was for 3 s.

Studies of microstructure and chemical composition were performed using FEI Magellan 400 scanning electron microscope (SEM) with energy dispersive X-ray spectroscopy (EDS) module. The survey was carried out in a high vacuum mode using a “through-lens” (TLD) detector at an accelerating voltages of 5–10 kV and high beam currents of 0.20–0.40 nA with magnification up to 65 000 ×. The size of grains was determined from analysis of SEM images within clear and defined grain boundaries using Nano Measure 1.2.5 software [24]. The type and parameters of crystal lattice were determined based on the full-profile analysis of the obtained diffraction patterns using DRON-3M diffractometer in CuK_α radiation at room temperature. The diffraction reflection patterns were recorded in the 2 theta-omega mode (scanning pitch of 0.02°, time at a point of 2 s). The analysis and refinement of X-ray data were performed by Rietveld method using JANA2006 software [25]. Lattice parameters and X-ray density were determined with an accuracy ±0.0001 Å and ±0.01 g/cm^3, respectively.

The frequency dependences of relative dielectric constant $\varepsilon_1(f)$ and loss tangent tan$\delta(f)$ were measured via dielectric spectroscopy [26] within low-frequency (LF) $f = 1\text{–}10^6$ Hz and ultra-high-frequency (HF) $f = 8.15\text{–}12.05$ GHz ranges at room temperature. An accuracy of determination of $\varepsilon_1(f)$ and tan$\delta(f)$ does not exceed 3 and 5% for LF, and 5 and 15% for ultra-HF ranges, respectively. The $\varepsilon_1(f)$ and tan$\delta(f)$ measurements in the LF range [27] were carried out using graphite powder rubbed homogeneously over the entire surface on both sides of the cylindrical samples (d = 8 mm and h = 2–3 mm).

3. Results and discussion

3.1. Structural properties

According to X-ray diffraction data, the single-phase $La_{0.5}R_{0.5}FeO_3$ samples crystallize in an orthorhombic structure with a *Pbnm* space group (No. 62). The absence of traces of the initial oxides indicates their complete polymorphic transformation. The results of a full-profile analysis of X-ray patterns are shown in Fig. 1(a–e). The high degree of fitting between the model and experimental X-ray patterns is confirmed by the goodness of fit (GOF) and/or Chi squared χ^2 values, which are related as $GOF^2 = \chi^2 = (R_{wp}/R_{exp})^2$ [28], where R_{exp} and R_{wp} are expected and weighted profile R factors. The lattice parameters and unit cell volumes are presented in Table 1. The obtained lattice parameters are in good agreement with the literature data [5,10–21]. A trend of a change in the lattice parameters remains depending on the type of substituting cations. A slight difference in the lattice parameters obtained by us and various authors is due to the use of different chemical methods for the synthesis of samples.

Using a linear dependence $y = k \cdot x + m$ for approximation of the experimental data (Table 1) and ionic radii, $x = r$, for R-cations [29], the crystal lattice parameters for the full-doped $La_{0.5}R_{0.5}FeO_3$ samples with R = Ce–Lu can be calculated. The fitting parameters and approximation results are shown in Fig. 2 and in Table S1 of Supplementary material (SM).

The dependences of the lattice parameters on the type of R-cation are consistent with the results obtained for the $Eu_{0.2}R_{0.8}FeO_3$ orthoferrites [30]. The decrease in the degree of octahedral distortion $S = 2\cdot(b-a)/(b+a)$ [31], observed with an increase in values of the radii of substituting R-cations, is due to a systematic increase in values of a and b lattice parameters in relation to a slight decrease in the values of $b-a$. The obtained data indicate that the distortion increases with decrease in the radius of the substituted R-cation.

Additionally, independent studies of structural distortions, such as: crystal lattice parameters (a, b, c), unit cell volume (V), orthorhombic distortion degree (S), and the ratio of the crystal lattice parameters (c/a) depending on the values of ionic radii for the $La_{0.5}R_{0.5}FeO_3$ (R = Ce–Lu) were conducted using SPuDS software [32]. The data obtained are presented in SM (see Fig. S1).

The volume values, calculated using SPuDS software, are approximately 2–4% higher than the values determined experimentally. However, the dynamics of their behavior depending on the type of R-cation is similar to the experimental data. The unit cell volume V_{Calc} and V_{Exp} of the samples decreases in the series of substituting cations from Ce^{3+} to Lu^{3+}. This is due to the 4f-compression effect caused by the size factor [33]. According to the calculated results, an increase in the volume of crystal lattice with an increase in radii of the substituted R^{3+}-cations is accompanied by a multidirectional change in the values of structural distortions S and ratio (c/a). The value of the orthorhombic deformation S decreases and a slight increase in the value of the c/a ratio is noted that is consistent with the results of experimental study. The calculated values of the global instability index (GII) and tolerance factor (t) (see Fig. 3) indicate a high stability of the crystal lattices of the $La_{0.5}R_{0.5}FeO_3$ samples. Even in the least stable lattice of the $La_{0.5}Lu_{0.5}FeO_3$ composition, the GII index does not exceed 0.15 u.v., and the value of t factor varies from 0.89 to 0.83, which is slightly less than the lower boundary value of the interval $0.87 < t < 0.99$ for the *Pbnm* lattice [32].

According to SEM data, the microstructure of the $La_{0.5}R_{0.5}FeO_3$ (R = Er, Dy, Gd, Sm, Nd) ceramics was studied for both external (outside) and internal (inside) surfaces (see Fig. 4). For any case, there are no appreciable traces of impurities or phase segregations on the surface and at the grain boundaries that additionally confirms a complete polymorphic transformation of initial oxides. For an external (outside) surface (see Fig. 4 (a), (c), (e), (g), (i)), an absence of clearly defined microstructure may be related to the preparation method of the $La_{0.5}R_{0.5}FeO_3$ ceramics synthesized under high P = 4 GPa as it was shown for $Eu_xBi_{1-x}FeO_3$ ceramics [23].

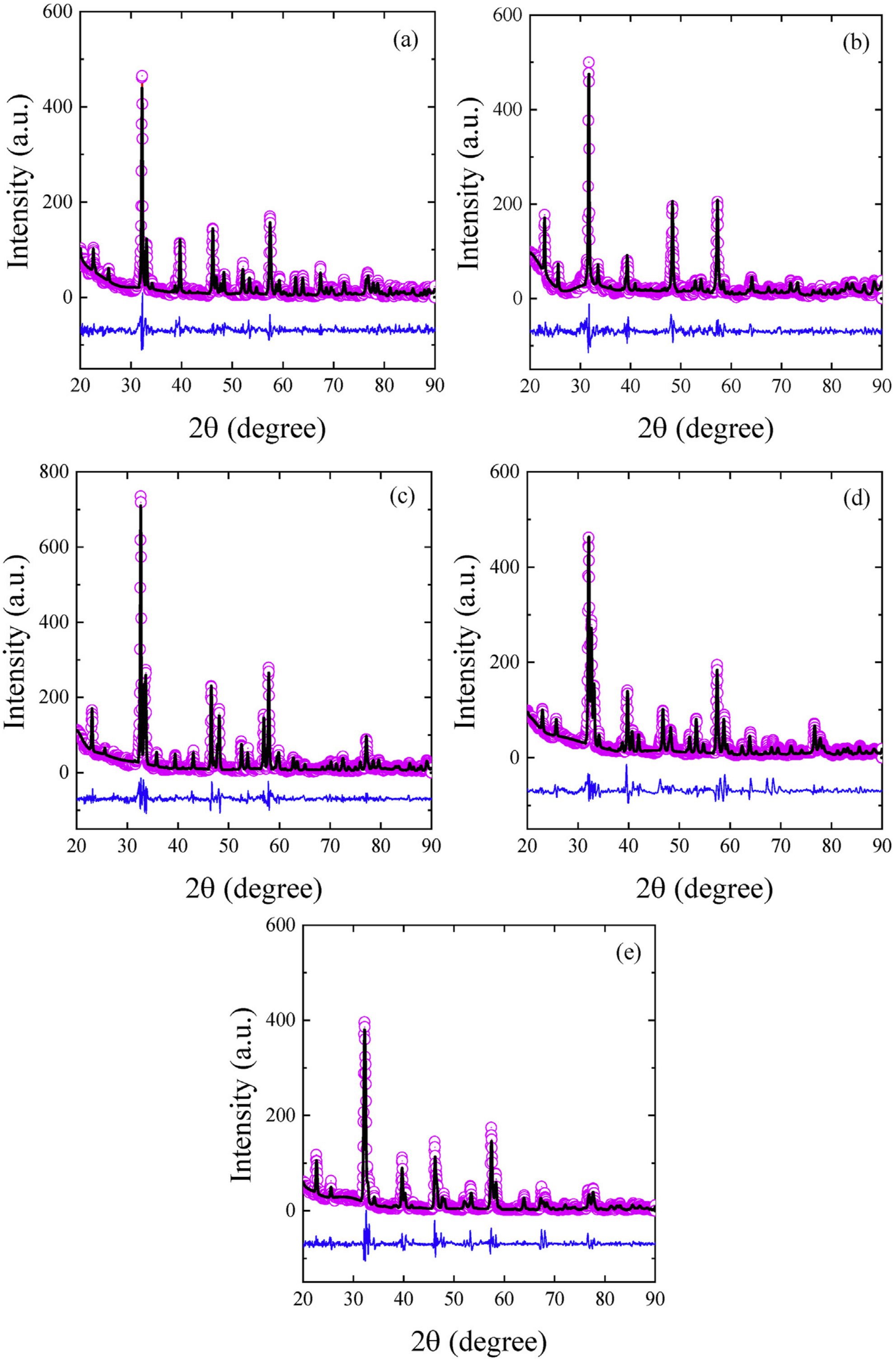

Fig. 1. X-ray patterns obtained at room temperature for the $La_{0.5}Er_{0.5}FeO_3$ (a), $La_{0.5}Dy_{0.5}FeO_3$ (b), $La_{0.5}Gd_{0.5}FeO_3$ (c), $La_{0.5}Sm_{0.5}FeO_3$ (d), and $La_{0.5}Nd_{0.5}FeO_3$ (e) samples.

For internal (inside) surface (see Fig. 4 (b), (d), (f), (h), (j)), the microstructure is well developed with high densification and well connected grains which grow from 133 nm for Er^{3+} to 570 nm for Nd^{3+} with an increase in the radius of *R*-cation. Usually, smaller grain size is ascribed to lower diffusion across the grain boundary during the sintering process [34]. In a first stage, the densification process occurs and then further grain growth is observed. Both processes are generally controlled by grain boundary diffusion rather than bulk diffusion. As it has been shown in Ref. [35], a similar grain size dependence of the radius of *R*-cation is observed for $BaCe_{0.9}Ln_{0.1}O_3$ ceramics with Ln = La, Nd, Sm, Gd, Tb, and Yb. It has been noted that, according to the space charge model [36], an enrichment of the trivalent dopant (in a sequence of La → Yb) at the grain boundary region generates a concentration gradient

Table 1
Lattice parameters (Å), unit cell volume (Å^3), GOF and χ^2, as well as X-ray density (g/cm^3) for the La$_{0.5}$$R_{0.5}FeO_3$ (R = Er, Dy, Gd, Sm, Nd) samples obtained by the Rietveld refinement of X-ray patterns.

Composition	d_x(g/cm^3)	Structural parameters and criteria of fit							
		a(Å)	b(Å)	c(Å)	V(Å^3)	GOF	χ^2	R_{exp} (%)	R_{wp} (%)
La$_{0.5}$Er$_{0.5}$FeO$_3$	7.32	5.3496	5.5543	7.8525	233.32	1.15	1.32	16.57	23.44
La$_{0.5}$Dy$_{0.5}$FeO$_3$	7.21	5.3306	5.6338	7.8163	234.74	1.05	1.10	14.66	19.95
La$_{0.5}$Gd$_{0.5}$FeO$_3$	7.12	5.3529	5.6575	7.7680	235.25	1.12	1.25	13.80	20.17
La$_{0.5}$Sm$_{0.5}$FeO$_3$	6.98	5.4238	5.5992	7.7875	236.50	1.17	1.37	14.55	21.38
La$_{0.5}$Nd$_{0.5}$FeO$_3$	6.85	5.4494	5.5655	7.8481	238.02	1.14	1.30	18.87	25.97

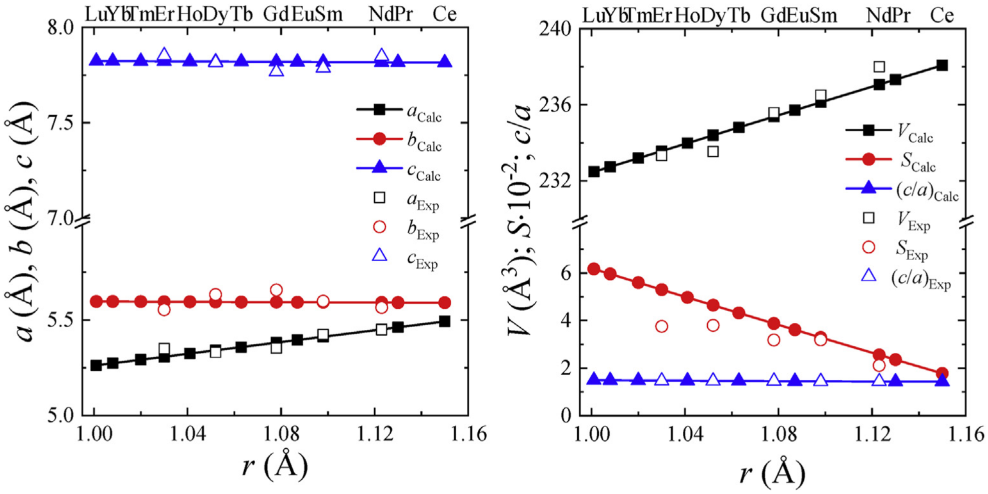

Fig. 2. Experimental (Exp) and calculated (Calc) dependences of the crystal lattice parameters (a, b, c), unit cell volume (V), orthorhombic distortion degree (S), and the ratio of the crystal lattice parameters (c/a) on the radius of R-cation.

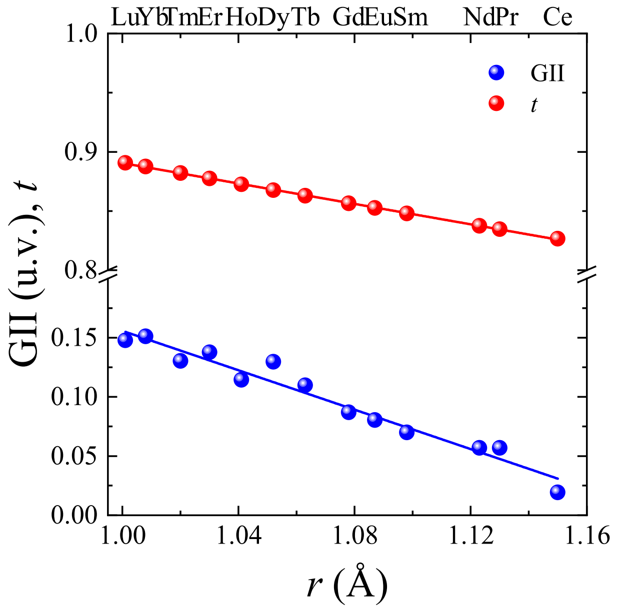

Fig. 3. Dependences of the global instability index (GII) and the Goldschmidt tolerance factor (t) on the radius of the R-cation calculated using the SPuDS program [32].

between the grain interior and grain boundary which decreases the mobility of cations along the grain boundary and, therefore, the densification and grain growth rate decrease. In our case, it may also suppose that an increase in the grain size from Er to Nd may be ascribed to higher diffusion across the grain boundary during the sintering process and increasing the mobility of cations along the grain boundary. However, more in-depth understanding of these processes occurring in the La$_{0.5}$$R_{0.5}FeO_3$ ceramics during the sintering process requires additional experimental studies. Additionally, the chemical composition of the La$_{0.5}$$R_{0.5}FeO_3$ (R = Er, Dy, Gd, Sm, Nd) samples and their stoichiometric ratio 0.5:0.5:1:3 were confirmed by EDS data (see Table S2 and Fig. S2).

3.2. Dielectric properties

The dielectric spectra of the samples are shown in Fig. 5. In the frequency range from 1 to 10^8 Hz, the real components of the dielectric constant $\varepsilon_1(\omega)$ and the dielectric loss tangent $\tan\delta_\varepsilon(\omega) = \varepsilon_2(\omega)/\varepsilon_1(\omega)$ are characterized by a relaxation type. In the formation of the dielectric response at LF, all possible mechanisms of dielectric polarization are involved. Their contribution varies from 10^4 to 10^5 at room temperature that is higher than in BaTiO$_3$ [37]. This is mainly due to the migration of charge carriers and their accumulation on the grain boundaries (see Fig. 4), defect structure and inhomogeneities that always occur in real polycrystalline samples [27]. High values of the ε_1 component can be also associated with low porosity, which leads to an increase in the effective contact area between crystallites (see Fig. 4). Moreover, the colossal dielectric response in the La$_{0.5}$$R_{0.5}FeO_3$ compositions depends on the following factors: (i) the presence of point defects, i.e. anion and cation vacancies [27,38,39]; (ii) the appearance of different valence iron ions [27,38,40]; (iii) preparation method of samples [19,23,27,41]; (iv) pressing pressure [38,41]; and (v) grain morphology [27,36,38]. It should be also noted that extreme conditions (cold pressing at high pressure P = 4 GPa for a short time of 1 min) used for obtaining ceramic samples should also affect the

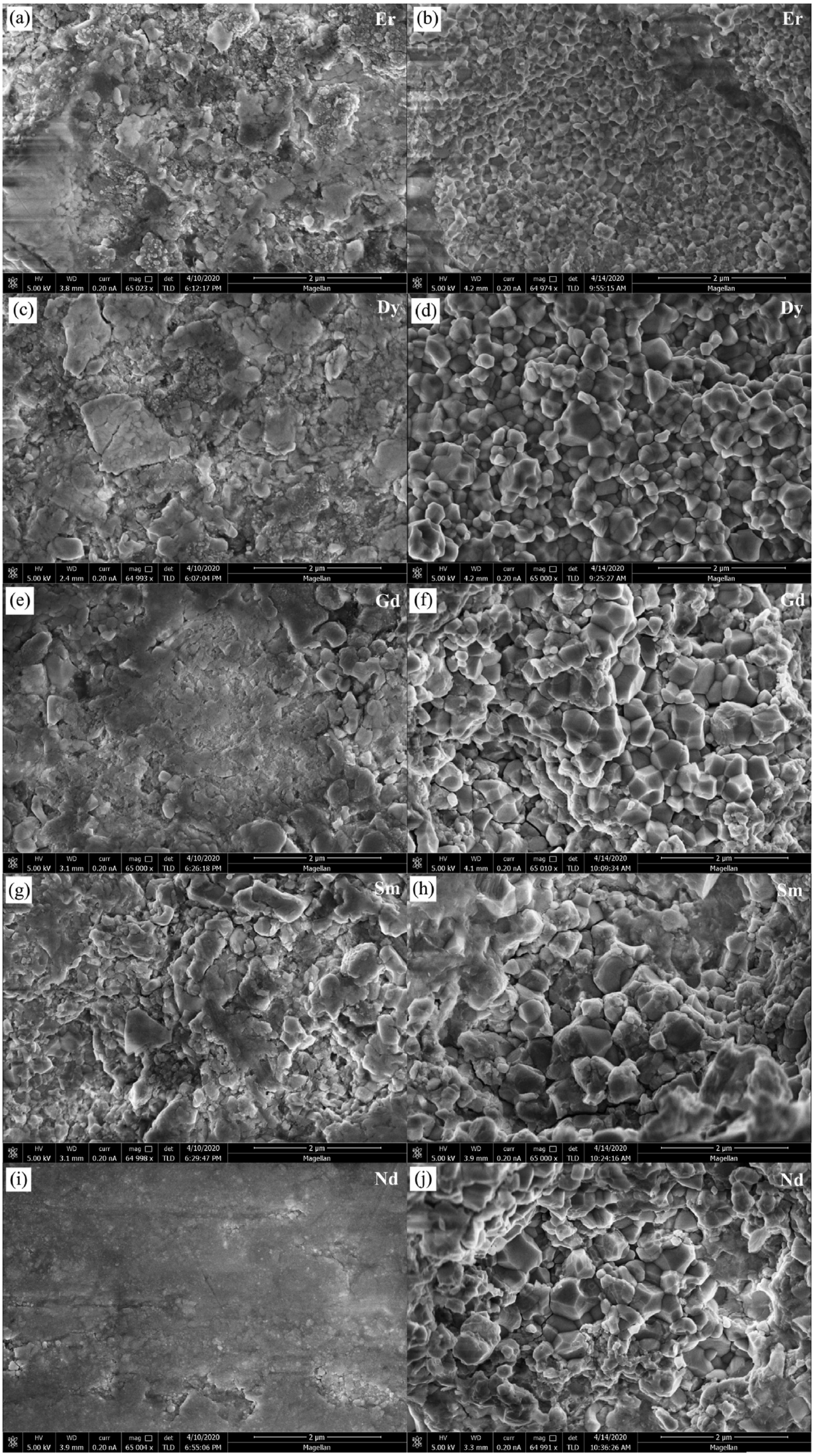

Fig. 4. SEM images obtained outside and inside for the $La_{0.5}R_{0.5}FeO_3$ ceramics with R = Er (a) and (b), Dy (c) and (d), Gd (e) and (f), Sm (g) and (h), Nd (i) and (j), respectively.

colossal dielectric response in the $La_{0.5}R_{0.5}FeO_3$ compositions due to a possible decrease in porosity, local heating, appearance of microstresses, and a change in oxygen amount. However, the confirmation of these factors requires additional experimental studies on valence state of ions and defect structure.

In the frequency range from 10^3 to 10^6 Hz, the dispersion region ε_1 is supposed to be associated with the valence change of iron ions as it was shown for a similar $Bi_{1-x}La_xFeO_{3-\delta}$ metal oxide using XPS method [27], i.e. with an electron hopping process between $Fe^{2+} \leftrightarrow Fe^{3+}$ ions occupying octahedral positions in the orthoferrite structure. An appearance of different valence iron ions Fe^{2+}/Fe^{3+} is associated with the availability of point defects of the vacancy type (cation $V^{(c)}$ and anion $V^{(a)}$ vacancies) in ABO_3 perovskite structure, and with a preparation method [27,38]. According to the established defect formation mechanism [27,33,38,42], the appearance of $V^{(a)}$ vacancies occurs upon heating of the samples and is caused by thermal dissociation of oxygen. The appearance of $V^{(c)}$ vacancies occurs upon cooling of the samples and is due to the greater mobility of the cation sublattice. As a result of the cyclic temperature changes during synthesis of the samples, a real structure of orthoferrites becomes imperfect and may contain $V^{(a)}$ and $V^{(c)}$ vacancies, the concentrations of which strongly depend on sintering temperature and synthesis conditions. In our case, the polycrystalline $La_{0.5}R_{0.5}FeO_3$ samples were synthesized at a medium temperature of 850 ± 50 °C close to a temperature of $t_{synth} = 850$ °C for $Bi_{1-x}La_xFeO_{3-\delta}$ [27], where the main contribution in an appearance of different valence iron ions was determined by $V^{(a)}$ vacancies. Therefore, taking into account an electroneutrality condition, the molar formula of a real orthoferrite can be written as $[La^{3+}_{0.50}R^{3+}_{0.50}]_A\{Fe^{3+}_{1-2\delta}Fe^{2+}_{2\delta}\}_B O^{2-}_{3-\delta}V^{(a)}_{\delta}$, where the concentration of Fe^{2+} ions increases with a decrease in the amount of oxygen "$O_{3-\delta}$", i.e. with an increase in the concentration of $V^{(a)}$ vacancies. In ideal case, without any point defects and in course of isovalent substitution of La^{3+} for R^{3+} ions, the molar formula will be $[La^{3+}_{0.50}R^{3+}_{0.50}]_A\{Fe^{3+}_{1.00}\}_B O^{2-}_{3.00}$, where there are no different valence iron ions.

As the frequency increases, a decrease in the dielectric constant is due to a decrease in the number of dipoles capable of following the rapid changes in the polarity of the applied alternating electric field. With further increase in the frequency, the values of ε_1 decrease and are quasi-stable 17–24 at 10^8 Hz due to elastic electron and ion polarizations. Above this frequency $f > 10^8$ Hz up to 10^{11} Hz, all samples demonstrate a frequency-independent behavior of dielectric functions.

The model spectra of the $\varepsilon^* = \varepsilon_1 + i\varepsilon_2$ components, which are in good agreement with the experimental data (see Fig. 5), can be described by the relations [27,43]:

$$\varepsilon_1 = \varepsilon_{hf} + \frac{\left(\varepsilon_s - \varepsilon_{hf}\right)\left[1 + (\omega\tau)^{1-\alpha}\sin(\pi\alpha/2)\right]}{1 + 2(\omega\tau)^{1-\alpha}\sin(\pi\alpha/2) + (\omega\tau)^{2(1-\alpha)}} + \frac{\left(\varepsilon_{s1} - \varepsilon_{hf\,1}\right)\left[1 + (\omega\tau_2)^{\gamma}\sin(\pi\gamma/2)\right]}{1 + 2(\omega\tau_2)\sin(\pi\gamma/2) + (\omega\tau_2)^{2\gamma}} + \frac{\sigma_1}{\varepsilon_0\omega^{\beta_1}}, \quad (1)$$

$$\varepsilon_2 = \frac{\left(\varepsilon_s - \varepsilon_{hf}\right)(\omega\tau)^{1-\alpha}\cos(\pi\alpha/2)}{1 + 2(\omega\tau)^{1-\alpha}\sin(\pi\alpha/2) + (\omega\tau)^{2(1-\alpha)}} + \frac{\left(\varepsilon_{s1} - \varepsilon_{hf1}\right)(\omega\tau_2)^{\gamma}\cos(\pi\gamma/2)}{1 + 2(\omega\tau_2)\sin(\pi\gamma/2) + (\omega\tau_2)^{2\gamma}} + \frac{\sigma_2}{\varepsilon_0\omega^{\beta_2}}, \quad (2)$$

where ε_s is the static dielectric constant, ε_{hf} is the HF dielectric constant, ε_0 is the vacuum permittivity, and σ is the conductivity. The α, β, and γ parameters characterize the distributions of the relaxation times τ determined in the first approximation from the condition $\omega_{max} \cdot \tau = 1$, where ω_{max} is the frequency corresponding to the maximum of $\tan\delta_\varepsilon$. The second and third terms in Eq. (1) are mathematical expressions describing the Debye model in different frequency intervals with the Cole-Cole and Cole-Davidson distributions of the relaxation times [44,45], respectively.

The second term in Eq. (1) can be related to the electron hopping mechanism between the $Fe^{2+} \leftrightarrow Fe^{3+}$ ions, which is in the frequency range from 10^4 to 10^7 Hz [46]. The third term in Eq. (1) describes the HF relaxation mechanism of the dielectric polarization, the nature of which has not been finally clarified. A possible mechanism of the dielectric polarization in a frequency range $< 10^4$ Hz is a motion of the walls of the magnetic domains [47] or/and a ferroelectric polarization [48,49]. In the LF limit, which is described by the last term in Eqs. (1) and (2), the large values of $\tan\delta_\varepsilon$ are due to the contributions of quasi-free carriers of the electric current to the dielectric polarization, i.e. the dielectric losses are related to the conductivity and accumulation of electric charge on the intercrystalline boundaries, inhomogeneities, and structural defects within a framework of the Maxwell-Wagner and Koops models [50]. The simulation results and model parameters are shown in Fig. 5 and Table S2.

Fig. 6 shows the dependences of the model parameters on the type of substitution R-cation for the $La_{0.50}R_{0.50}FeO_3$ (R = Er, Gd, Sm, Nd). As it can be seen, almost linear dependences are obtained for all model parameters. An assumption about a linear behaviour of the model parameters is indirectly confirmed by the change in the lattice parameters and unit cell volume calculated for the $La_{0.50}R_{0.50}FeO_3$ (see Fig. 2), as well as other data for RE orthoferrites [51] and double orthoferrites $Eu_{0.80}R_{0.20}FeO_3$ [30]. In all cases, a monotonic decrease in the crystal lattices from La to Lu depending on the type of R-cation is observed. A slight difference in lattice parameters is associated with various synthesis conditions used in papers.

While approximation of the data presented in Fig. 6 by a linear dependence $y = k \cdot x + m$ ($x = r$ is the radius of the R-cation), the parameters of the model spectra for the $La_{0.50}R_{0.50}FeO_3$ samples (R = Lu–Ce) can be recalculated (see Fig. 7).

The presence of different valence Fe^{3+} and Fe^{2+} cations occupying equivalent crystallographic positions leads to the formation of dipoles, the rotation and displacement of which causes orientational polarization. The inertia of this mechanism leads to a decrease in polarization with an increase in a frequency of the external electric field. At high frequencies, the values of the dielectric loss tangent decrease from 0.01 to 0.001, depending on the composition (see Fig. 7(a)). The dispersion of losses in the range from 10^5 to 10^7 Hz demonstrates the relaxation behavior. In the LF limit, high-resistance grain boundaries obstruct the polarization processes associated with the movement of charges, and, as a result, the dielectric losses increase. As grain size decreases (see Fig. 4), the dielectric loss tangent $\tan\delta_\varepsilon$ increases in a sequence of Ce → Lu (see Fig. 7(a)). At the same time, the decrease in the grain size causes an increase in the dielectric constant ε_1 within the LF limit (see Fig. 7(b)) due to accumulation of electric charge on the grain boundaries. A similar behaviour of dielectric constant and dielectric loss tangent depending on the grain size was observed for the Fe-based $Bi_{1-x}La_xFeO_{3-\delta}$ ($0 \le x \le 0.5$) ceramics [27]. The frequency dependences of the dielectric constant (see Fig. 7(b)) have the form which is typical for polydisperse compounds with Debye relaxation. This can be explained using the Cole–Cole diagrams (see Fig. 8) due to the presence of dielectric polarization mechanisms with a distribution of relaxation times [45]. As can be seen from Fig. 8 (straight lines in LF range), this diagram is typical for dielectrics which have losses associated with the migration of quasi-free electric charge carriers and described by the last terms in Eqs.

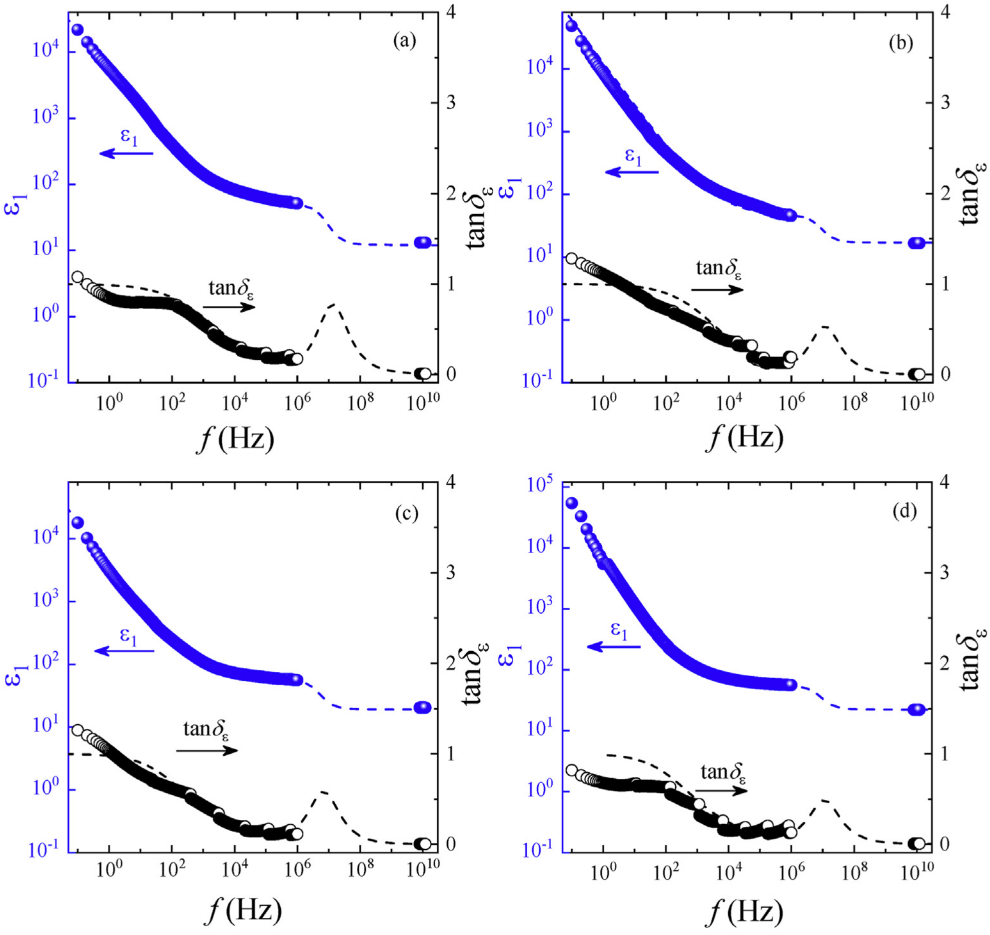

Fig. 5. Experimental (points) and model (dashed lines) frequency dependences of the real dielectric components ε_1 and the dielectric loss tangent $\tan\delta_\varepsilon$ of the $La_{0.50}R_{0.50}FeO_3$ samples with R = Er (a), Gd (b), Sm (c), Nd (d).

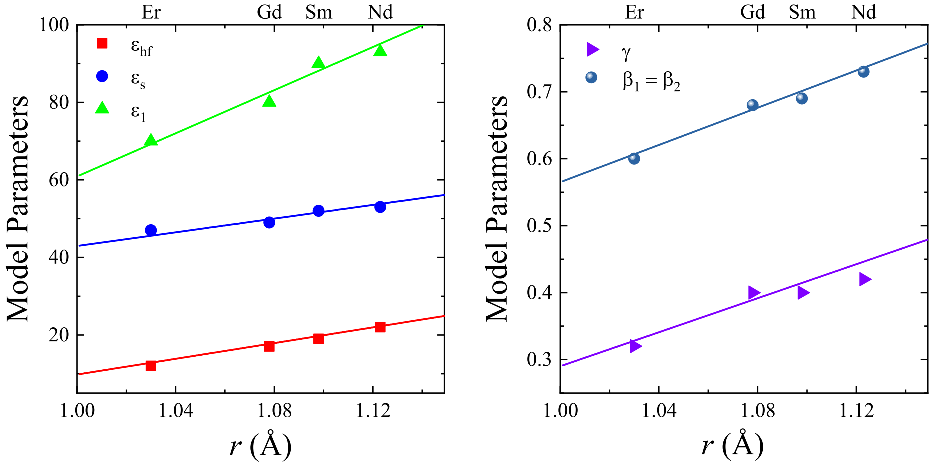

Fig. 6. Dependences of the model parameters on the type of R-cation for the $La_{0.50}R_{0.50}FeO_3$ (R = Nd, Sm, Gd, Er) orthoferrites.

(1) and (2). In the general case, this contribution depends on the grain size, since it is associated with the migration of charges inside the grains and with their accumulation at the grain boundaries. As grain size reduces with a decrease in radius of R-cation (see Fig. 4), the dielectric losses increase (a raise in the tilt angle of straight lines in Fig. 8) due to an increase in the intergranular area. This contribution prevails in LF range and can mask other polarization mechanisms. In the HF limit, the semicircles are displaced depending on the type of R-cation and are decreased with an increase in the grain size, which confirms a decrease in dielectric losses due to migration of quasi-free charge carriers inside homogeneously larger grains. In an ideal dielectric material without any losses, the “radius” of the semicircle is defined as half the difference (ε_s - ε_{hf}), and the center of the semicircle at one relaxation time is on

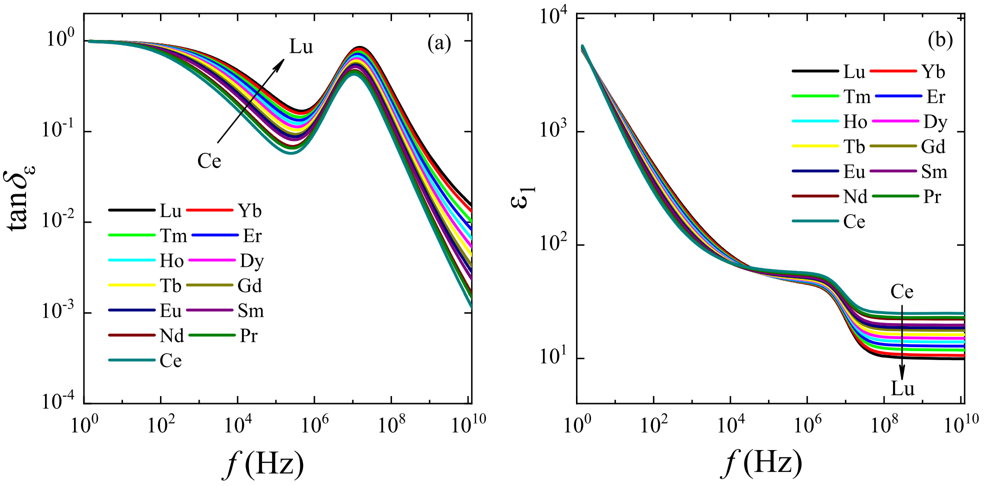

Fig. 7. Model spectra of the dielectric loss tangent (a) and dielectric constant (b) for the $La_{0.50}R_{0.50}FeO_3$ (R = Ce–Lu).

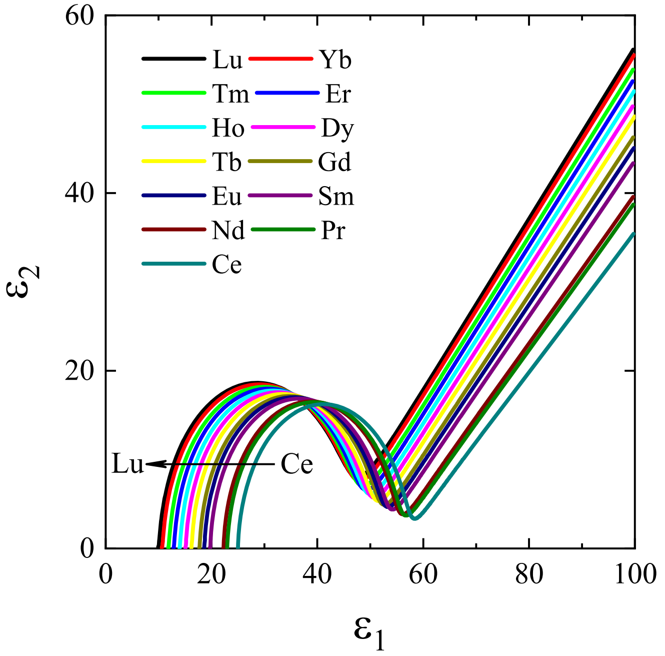

Fig. 8. Cole–Cole diagrams based on the model spectra of the real (ε_1) and imaginary (ε_2) components of the complex dielectric constant ε^* for the $La_{0.50}R_{0.50}FeO_3$ (R = Ce–Lu).

the ε_1 axis. In a real dielectric material with several polarization mechanisms, the semicircle can be deformed and characterized by the distribution of relaxation times. In such materials, the semicircle is asymmetric, and its shape is determined by the coexistence of various mechanisms of dielectric polarization that can be clearly seen from Fig. 8 for the studied samples.

3.3. Electrical module analysis

In the LF range, the dielectric constant is masked by the shunting effect of the composition conductivity. The intensity of electron exchange is structurally dependent and is determined by the degree of overlap of the electron orbitals of O-2*p* and Fe-3*d*, which correlates with changes in the values of the bond angles of Fe–O–Fe and the lengths of the interionic bonds of Fe–O, La(*R*)–O. As it can be seen from Fig. 9, a relatively small increase in the lengths of La(*R*)–O(1,2) and a decrease in the lengths of La(*R*)–O(3,4) with a reduce in the radii of the *R*-cations cause a decrease in the values of the valence angles, which leads to less overlap of the electron orbitals. This leads to a decrease in the conductivity. At the same time, internal structural distortions in the samples associated with the tilting of the FeO_6 octahedra increase, which can lead to an increase in the ac conductivity, specially, in compositions with a smaller radius of *R*-cations. Both mechanisms are interconnected and effect by the complex way the change in the conductivity, which in LF range has a shunting effect and makes it difficult to interpret the results of measured dielectric functions.

While analyzing the LF dielectric response, the behavior of the $M_1 = \varepsilon_1/[(\varepsilon_1)^2+(\varepsilon_2)^2]$ and $M_2 = \varepsilon_2/[(\varepsilon_1)^2+(\varepsilon_2)^2]$ components of the complex electric module $M^* = M_1+i\cdot M_2$ are considered [52]. These characteristics reflect the relaxation of the electric field in the substance. An analysis of the frequency dependences of $M_1(\omega)$ and $M_2(\omega)$, where $\omega = 2\pi f$, allows to study a difference in the resistivity of the crystallites. The calculated frequency dependences of $M_1(\omega)$ and $M_2(\omega)$, as well as the Cole-Cole diagrams are presented in Figs. 10 and 11.

The values of M_1 increase with a rise in the frequency and pass through an intermediate maximum in the range from 10^4 to 10^5 Hz. At frequencies greater than 10^8 Hz, the M_1 reaches saturation. In the frequency range 10^3–10^8 Hz, two peaks of the M_2 reflect two relaxation processes. The first one (in the LF range) corresponds to grain-boundary effects, and the second one corresponds to the movements of quasi-free charge carriers within grains. The data shown in Fig. 10 demonstrate shifts of the M_2 peaks toward LF with an increase in radius of the *R*-cation. It testifies a decrease in the relaxation rates and an increase in relaxation times of both processes from $\tau = 1.95\cdot10^{-4}$ s ($R = Er^{3+}$) to $8.56\cdot10^{-4}$ s ($R = Nd^{3+}$) in the LF range and from $\tau = 0.94\cdot10^{-8}$ s ($R = Er^{3+}$) to $1.63\cdot10^{-8}$ s ($R = Nd^{3+}$) in the HF range, which can be associated with an increase in the unit cell volume (see Fig. 2) and a growth in the grain size of the $La_{0.50}R_{0.50}FeO_3$ samples from 133 nm ($R = Er^{3+}$) to 570 nm ($R = Nd^{3+}$) (see Fig. 4). The Cole-Cole diagrams (see Fig. 11) are characterized by the presence of two asymmetric relaxation peaks. Relatively low values of electrical modules indicate a small contribution of electrodes to the mechanism of electrical conductivity. Local minima in the frequency range 10^5–10^6 Hz and maxima at a frequency of ~ 10^7 Hz in the spectra $\tan\delta_\varepsilon(f)$ (see Fig. 7(a)) and in the spectra of $M_2(f)$ (Fig. 10(b)) practically coincide. It should be also noted that the same behaviour is observed in the

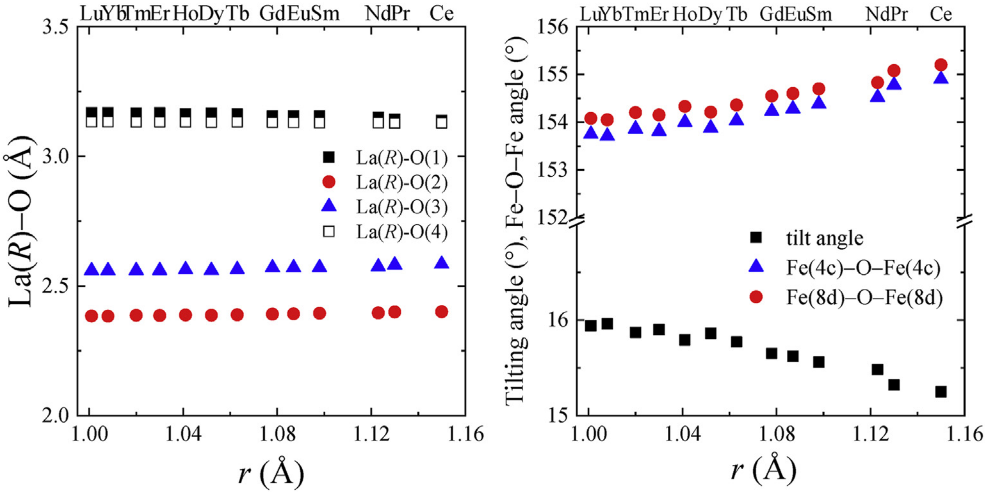

Fig. 9. Dependences of the crystal and chemical parameters on the radius of the *R*-cation calculated using the SPuDS program.

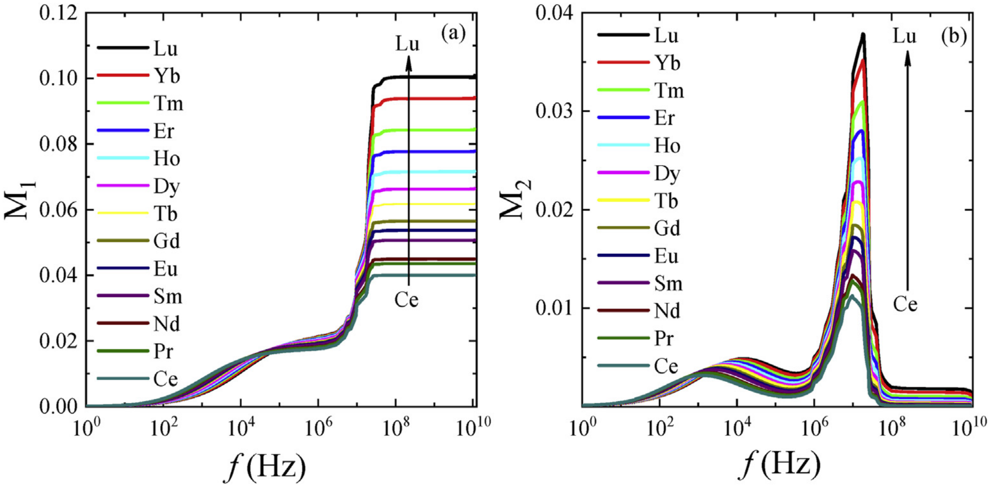

Fig. 10. Frequency dependences of the real, M_1, (a) and imaginary, M_2, (b) components of the complex electric module for the $La_{0.50}R_{0.50}FeO_3$ (R = Ce–Lu) orthoferrites.

dependences $\varepsilon_2(f) = \varepsilon_1(f)\cdot\tan\delta_\varepsilon(f)$. This confirms that the processes of conduction and relaxation are regulated by the same defects in the studied samples.

In the formation of the dielectric constant in the HF limit (an optical range), the ionic and electronic mechanisms of dielectric polarization are the main. The LF mechanisms of dielectric polarization are eliminated at such high frequencies. An analysis of the structural data indicates that the lattice parameters of the $La_{0.50}R_{0.50}FeO_3$ samples are systematically changed due to the 4*f*-effect compression. However, structural factors are weakly sensitive to changes in the composition. This allows supposing that changes in dielectric properties are mainly determined by the difference in the polarizability of the substituted *R*-cations and O^{2-} anions. The dielectric constant decreases while replacement of lanthanum cations by *R*-cations in the $La_{0.50}R_{0.50}FeO_3$. The results of calculation of the electron polarizability α for *R*-cations [53,54] indicate their monotonic growth with an increase in ionic radii. Maximum polarizability is observed for La^{3+} cations. Taking into account the additive feature of polarizability, it is possible to calculate the effective polarizability (α_{eff}) as the half-sum of $\alpha_{La^{3+}}$ and $\alpha_{R^{3+}}$ for all compositions. The dependence of the dielectric constant on the type of *R*-cation calculated in the HF limit as well as the polarizability of $\alpha_{R^{3+}}$ and α_{eff} calculated on the basis of the data [53] are shown in Fig. 12. Substitution of La^{3+} cations with *R*-cations from Lu to Ce leads to an increase in α_{eff}, which should increase the values of the real dielectric components in the HF limit that is in good agreement with Fig. 6 and Table S3.

4. Conclusions

A solid-state reaction method under cold pressing at high pressure $P = 4$ GPa was used to prepare the rare-earth orthoferrite $La_{0.50}R_{0.50}FeO_3$ ceramics with R = Nd, Sm, Gd, Dy, and Er. Structural, microstructural, and dielectric properties of $La_{0.50}R_{0.50}FeO_3$ ceramics were studied comprehensively. Using a linear law of approximation for describing experimental data, the crystal-chemical characteristics and dielectric parameters were determined for full number of substitutions in the $La_{0.50}R_{0.50}FeO_3$ with R = Ce–Lu. With a decrease in the radius of *R*-cation from Ce to Lu, a decrease in the lattice cell volume, and an increase in orthorhombic distortion degree, global instability index and Goldschmidt tolerance factor are observed. The microstructure of the $La_{0.50}R_{0.50}FeO_3$ ceramics is well developed with high densification and well connected grains, the average size of which grows with an increase in

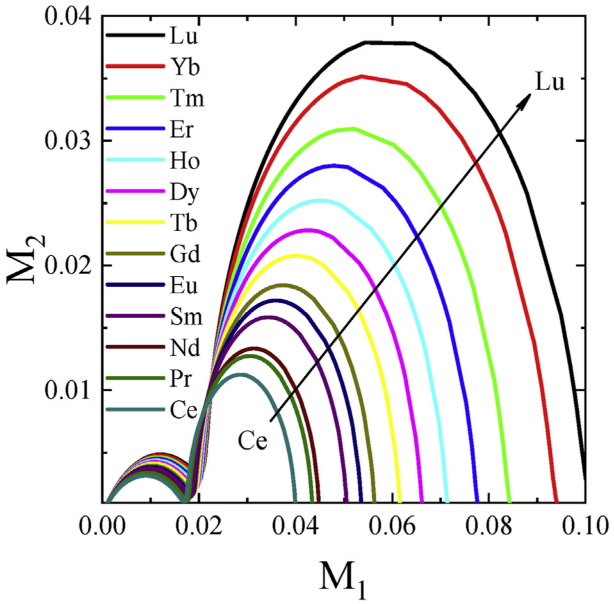

Fig. 11. Cole-Cole diagrams based on the model spectra of the real (M_1) and imaginary (M_2) components of the complex electric module M* for the $La_{0.50}R_{0.50}FeO_3$ (R = Ce–Lu) orthoferrites.

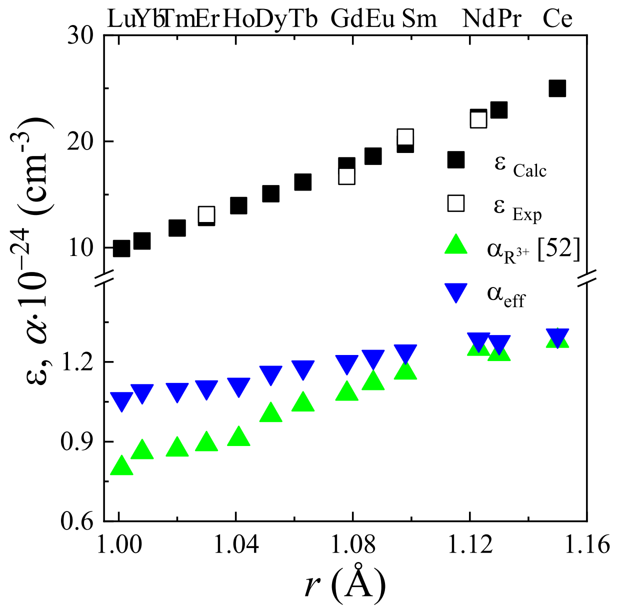

Fig. 12. Dependences of the experimental (ε_{Exp}) and calculated (ε_{Calc}) dielectric constants in HF limit, as well as polarizability of R-cations ($\alpha_{R^{3+}}$) and (α_{eff}).

the radius of R-cation. According to dielectric spectroscopy data, the ceramic $La_{0.50}R_{0.50}FeO_3$ samples demonstrate the colossal values of dielectric constant and relatively small values of dielectric loss tangent in a low-frequency limit that is caused by the migration of weakly coupled (quasi-free) charge carriers and their accumulation at grain boundaries. With decrease in the radius of R-cation from Ce to Lu, the components of the complex electric module (M_1 and M_2) and dielectric loss tangent ($\tan\delta_\varepsilon$) increase in contrast to decreasing components of the dielectric constants (ε_s, ε_{hf}, and ε_1) in a high-frequency range. All calculated and defined values on structural and dielectric characteristics for full number of substitutions in the $La_{0.50}R_{0.50}FeO_3$ orthoferrites with R = Ce–Lu are in good agreement with experimental data for the prepared $La_{0.50}R_{0.50}FeO_3$ ceramics with R = Nd, Sm, Gd, Dy, and Er which were taken as a basis. The obtained results can be useful for using promising method of preparation under high pressure to synthesize double rare-earth orthoferrite-based ceramic materials with colossal dielectric constant at room temperature.

Declaration of competing interest

The authors declare that they have no known competing financial interests or personal relationships that could have appeared to influence the work reported in this paper.

CRediT authorship contribution statement

I.I. Makoed: Conceptualization, Methodology, Project administration, Software, Supervision, Visualization, Writing - original draft. **N.A. Liedienov:** Data curation, Investigation, Project administration, Writing - review & editing. **A.V. Pashchenko:** Data curation, Formal analysis, Methodology. **G.G. Levchenko:** Formal analysis, Project administration, Resources, Supervision. **D.D. Tatarchuk:** Data curation, Investigation, Validation. **Y.V. Didenko:** Data curation, Investigation, Validation. **A.A. Amirov:** Conceptualization, Data curation, Formal analysis, Validation. **G.S. Rimski:** Data curation, Formal analysis, Validation. **K.I. Yanushkevich:** Conceptualization, Data curation, Formal analysis.

Acknowledgments

This work was performed within the framework of State Scientific Research Program 2016–2020 “Physical materials science, new materials and technology” (“Material Science and technology of materials” subprogram, task No. 1.35), and partially supported by The Thousand Talents Program for Foreign Experts program of China (project WQ20162200339) and Grant of NAS of Ukraine for research laboratories/groups of young scientists of NAS of Ukraine in 2020–2021 (No. 08/01-2020).

Appendix A. Supplementary data

Supplementary data to this article can be found online at https://doi.org/10.1016/j.jallcom.2020.155859.

References

[1] M.K. Warshi, V. Mishra, A. Sagdeo, V. Mishra, R. Kumar, P.R. Sagdeo, Structural, optical and electronic properties of $RFeO_3$, Ceram. Int. 44 (2018) 8344–8349.
[2] S.A. Solopan, O.I. V'yunov, A.G. Belous, A.I. Tovstolytkin, L.L. Kovalenko, Magnetoelectric effect in composite structures based on ferroelectric–ferromagnetic perovskites, J. Eur. Ceram. Soc. 30 (2010) 259–263.
[3] I. Fita, A. Wisniewski, R. Puzniak, E.E. Zubov, V. Markovich, G. Gorodetsky, Common exchange-biased spin switching mechanism in orthoferrites, Phys. Rev. B 98 (2018), 094421.
[4] P. Głuchowski, K. Oganisian, R. Tomala, A. Łukowiak, D. Karpinsky, D. Alikin, A. Kholkin, W. Stręk, Optical, dielectric and magnetic properties of $La_{1-x}Nd_xFeO_3$ powders and ceramics, Ceram 2 (2019) 1–12.
[5] X.-P. Xiang, L.-H. Zhao, B.-T. Teng, J.-J. Lang, X. Hu, T. Li, Y.-A. Fang, M.-F. Luo, J.-J. Lin, Catalytic combustion of methane on $La_{1-x}Ce_xFeO_3$ oxides, Appl. Surf. Sci. 276 (2013) 328–332.
[6] D.K. Li, D. Wang, F. Wu, T. Xie, T. Li, Surface electronic states and photovoltage gas-sensitive characters of nanocrystalline $LaFeO_3$, Mater. Chem. Phys. 64 (2000) 269–272.
[7] X. Li, C. Tang, M. Ai, L. Dong, Z. Xu, Controllable synthesis of pure-phase rare-earth orthoferrites hollow spheres with a porous shell and their catalytic performance for the CO + NO reaction, Chem. Mater. 22 (2010) 4879–4889.
[8] Y.K. Jeong, J.-H. Lee, S.-J. Ahn, H.M. Jang, Temperature-induced magnetization reversal and ultra-fast magnetic switch at low field in $SmFeO_3$, Solid State Commun. 152 (2012) 1112–1115.
[9] L. Hou, L. Shi, J. Zhao, S. Zhou, S. Pan, X. Yuan, Y. Xin, Room-temperature multiferroicity in $CeFeO_3$ ceramics, J. Alloys Compd. 797 (2019) 363–369.

[10] R. Maity, M.S. Sheikh, A. Dutta, T.P. Sinha, Visible light driven photocatalytic activity of granular Pr doped $LaFeO_3$, J. Electrn. Mater. 48 (2019) 4856–4865.

[11] S. Chanda, S. Saha, A. Dutta, A.S. Mahapatra, P.K. Chakrabarti, U. Kumar, T.P. Sinha, Multiferroicity in $La_{1/2}Nd_{1/2}FeO_3$ nanoparticles, Solid State Sci. 37 (2014) 55–63.

[12] A.P.B. Selvadurai, V. Pazhanivelu, C. Jagadeeshwaran, R. Murugaraj, P.M.M. Gazzali, G. Chandrasekaran, An analysis on structural and magnetic properties of $La_{1-x}RE_xFeO_3$ ($x=0.0$ and 0.5, RE = Nd, Sm and Gd) nanoparticles, Appl. Phys. 123 (2017) 13.

[13] S. Ekaphan, K. Attaphol, P. Sumalin, H. Sitchai, P. Thanin, Investigation of structural, morphological, optical, and magnetic properties of Sm-doped $LaFeO_3$ nanopowders prepared by sol–gel method, J. Sol Gel Technol. 81 (2017) 483–492.

[14] S.A. Hosseini, M. Taghi, S. Sorkhani, L.K. Ahmadi, A. Alemi, A. Niaei, D. Salari, Synthesis, characterization, and catalytic activity of nanocrystalline $La_{1-x}Eu_xFeO_3$ during the combustion of toluene, Chin. J. Catal. 32 (2011) 1465–1468.

[15] R.J. Wiglusz, K. Kordek, M. Małecka, A. Ciupa, M. Ptak, R. Pazik, P. Pohlc, D. Kaczorowskia, A new approach in the synthesis of $La_{1-x}Gd_xFeO_3$ perovskite nanoparticles – structural and magnetic characterization, Dalton Trans. 44 (2015) 20067–20074.

[16] B. Bashir, M.F. Warsi, M.A. Khan, M.N. Akhtar, Z.A. Gilani, I. Shakir, A. Wadood, Rare earth Tb^{3+} doped $LaFeO_3$ nanoparticles: new materials for high frequency devices fabrication, Ceram. Int. 41 (2015) 9199–9202.

[17] A. Mitra, A.S. Mahapatra, A. Mallick, A. Shaw, M. Ghosh, P.K. Chakrabarti, Simultaneous enhancement of magnetic and ferroelectric properties of $LaFeO_3$ by co-doping with Dy^{3+} and Ti^{4+}, J. Alloys Compd. 726 (2017) 1195–1204.

[18] A.S. Mahapatra, A. Mitra, A. Mallick, M. Ghosh, P.K. Chakrabarti, Enhanced magnetic property and phase transition in Ho^{3+} doped $LaFeO_3$, Mater. Lett. 169 (2016) 160–163.

[19] S. Katba, S. Jethva, G. Panchal, R.J. Choudhary, D.M. Phase, D.G. Kuberkar, Studies on electronic structure and dielectric properties of La-doped $ErFeO_3$ orthoferrites, J. Alloys Compd. 789 (2019) 814–824.

[20] S. Leelashree, P.D. Babu, S. Srinath, Effect of La doping on dielectric and magnetic properties of room temperature multiferroic $LuFeO_3$, in: AIP Conference Proceed. 1953, 2018, p. 120076.

[21] S. Leelashree, S. Srinath, Investigation of structural, ferroelectric, and magnetic properties of La-doped $LuFeO_3$ nanoparticles, J. Supercond. Nov. Magnetism 33 (2019) 1587–1591, https://doi.org/10.1007/s10948-019-5114-4.

[22] I.I. Makoed, A.F. Revinskii, Specific features of the evolution of magnetic properties of bismuth ferrite modified with rare-earth element cations, Phys. Solid State 57 (2015) 1787–1792.

[23] I.I. Makoed, A.A. Amirov, N.A. Liedienov, A.V. Pashchenko, K.I. Yanushkevich, D.V. Yakimchuk, E.YuAmirov Kaniukov, Evolution of structure and magnetic properties in $Eu_xBi_{1-x}FeO_3$, J. Magn. Magn Mater. 489 (2019) 165379, https://doi.org/10.1016/j.jmmm.2019.165379.

[24] Z. Wei, A.V. Pashchenko, N.A. Liedienov, I.V. Zatovsky, D.S. Butenko, Q. Li, I.V. Fesych, V.A. Turchenko, E.E. Zubov, P.Yu Polynchuk, V.G. Pogrebnyak, V.M. Poroshin, G.G. Levchenko, Multifunctionality of lanthanum-strontium manganite nanopowder, Phys. Chem. Chem. Phys. 22 (2020) 11817, https://doi.org/10.1039/D0CP01426E.

[25] V. Petricek, M. Dusek, L. Palatinus, Crystallographic computing system JANA2006: general features, Zeitschrift Fur Kristallographie crystal, Mater 229 (2014) 5.

[26] D.D. Tatarchuk, V.I. Molchanov, V.M. Pashkov, A.S. Franchuk, Microwave dielectric measurement methods on the base of the composite dielectric resonator, in: 2015 IEEE 35th Intern. Conferen. Electron. Nanotechn. ELNANO, Kyiv, Ukraine, 2015, pp. 231–234.

[27] N.A. Liedienov, A.V. Pashchenko, V.A. Turchenko, V.Ya Sycheva, A.V. Voznyak, V.P. Kladko, A.I. Gudimenko, D.D. Tatarchuk, Y.V. Didenko, I.V. Fesych, I.I. Makoed, A.T. Kozakov, G.G. Levchenko, Liquid-phase sintered bismuth ferrite multiferroics and their giant dielectric constant, Ceram. Int. 45 (2019) 14873–14879, https://doi.org/10.1016/j.ceramint.2019.04.220.

[28] B.H. Toby, R factors in Rietveld analysis: how good is good enough? Powder Diffr. 21 (2006) 67–70, https://doi.org/10.1154/1.2179804.

[29] R.D. Shannon, Revised effective ionic radii and systematic studies of interatomic distances in halides and chalcogenides, Acta Crystallogr. A. 32 (1976) 751–767.

[30] X. Liu, M. Jin, C. Zhang, Mössbauer spectroscopy study on double rare-earth orthoferrites $Eu_{0.2}R_{0.8}FeO_3$ (R = rare earth), J. Appl. Phys. 71 (1992) 5111–5114.

[31] M. Ain, J.-M. Delrieu, A. Menelle, G. Parette, J. Jegoudez, Orthorhombicity and oxygen uptake by $YBa_2Cu_3O_{6+x}$, J. Phys. France. 50 (1989) 1455–1461.

[32] M.W. Lufaso, P.M. Woodward, The prediction of the crystal structures of perovskites using the software program SPuDS, Acta Crystallogr. 57 (2001) 725–738.

[33] A.V. Pashchenko, V.P. Pashchenko, V.K. Prokopenko, V.A. Turchenko, YuF. Revenko, A.S. Mazur, V.Ya Sycheva, N.A. Liedienov, V.G. Pitsyuga, G.G. Levchenko, Role of structure imperfection in the formation of the magnetotransport properties of rare-earth manganites with a perovskite structure, J. Exp. Theor. Phys. 124 (2017) 100–113, https://doi.org/10.1134/S1063776116150127.

[34] M. Amsif, D. Marrero-López, J.C. Ruiz-Morales, S. Savvin, P. Núñez, Low temperature sintering of $LaNbO_4$ proton conductors from freeze-dried precursors, J. Eur. Ceram. Soc. 32 (2012) 1235–1244, https://doi.org/10.1016/j.jeurceramsoc.2011.11.027.

[35] M.D. Amsif, J.C. Ruiz-Morales, S.N. Savvin, M. Gabás, P. Marrero-Lopez Nunez, Influence of rare-earth doping on the microstructure and conductivity of $BaCe_{0.9}Ln_{0.1}O_{3-\delta}$ proton conductors, Power Sources 196 (2011) 3461–3469, https://doi.org/10.1016/j.jpowsour.2010.11.120.

[36] X. Guo, R. Waser, Electrical properties of the grain boundaries of oxygen ion conductors: acceptor-doped zirconia and ceria, Prog. Mater. Sci. 51 (2006) 151–210, https://doi.org/10.1016/j.pmatsci.2005.07.001.

[37] H.Z. Guo, Ya Mudryk, M.I. Ahmad, X.C. Pang, L. Zhao, M. Akinc, V.K. Pecharsky, N. Bowler, Z.Q. Lin, X. Tan, Structure evolution and dielectric behavior of polystyrene-capped barium titanate nanoparticles, J. Mater. Chem. 22 (2012) 23944.

[38] A.V. Pashchenko, N.A. Liedienov, Quanjun Li, D.D. Tatarchuk, V.A. Turchenko, I.I. Makoed, V.Ya Sycheva, A.V. Voznyak, V.P. Kladko, A.I. Gudimenko, Y.V. Didenko, A.T. Kozakov, G.G. Levchenko, Structure, non-stoichiometry, valence of ions, dielectric and magnetic properties of single-phase $Bi_{0.9}La_{0.1}FeO_{3-\delta}$ multiferroics, J. Magn. Magn Mater. 483 (2019) 100–113, https://doi.org/10.1016/j.jmmm.2019.03.095.

[39] S. Jethva, S. Katba, M. Udeshi, B. Vyas, H. Kundalia, P. Trivedi, M. Vagadia, D.G. Kuberkar, Studies on the structure and dielectric properties of Ca-doped $BiFeO_3$ multiferroics, Ferroelectrics 516 (2017) 106–116, https://doi.org/10.1080/00150193.2017.1362293.

[40] Majid Abdellahi, Ali Shokrollah Abhari, Maryam Bahmanpour, Preparation and characterization of orthoferrite $PrFeO_3$ nanoceramic, Ceram. Int. 42 (4) (2016) 4637–4641, https://doi.org/10.1016/j.ceramint.2015.12.027.

[41] Q.H. Jiang, C.W. Nan, Z.J. Shen, Synthesis and properties of multiferroic La-modified $BiFeO_3$ ceramics, J. Am. Ceram. Soc. 89 (2006) 2123–2127, https://doi.org/10.1111/j.1551-2916.2006.01062.x.

[42] A.V. Pashchenko, V.P. Pashchenko, V.K. Prokopenko, YuF. Revenko, YuS. Prylipko, N.A. Ledenev, G.G. Levchenko, V.P. Dyakonov, H. Szymczak, Influence of structure defects on functional properties of magnetoresistance $(Nd_{0.7}Sr_{0.3})_{1-x}Mn_{1+x}O_3$ ceramics, Acta Mater. 70 (2014) 218–227, https://doi.org/10.1016/j.actamat.2014.02.014.

[43] K. Majhi, B.S. Prakash, K.B.R. Varma, Extreme values of relative permittivity and dielectric relaxation in Sr_2SbMnO_6 ceramics, J. Phys. D Appl. Phys. 40 (2007) 7128–7135.

[44] K.S. Cole, R.H. Cole, Dispersion and absorption in dielectrics I. Alternating current characteristics, J. Chem. Phys. 9 (1941) 341–351.

[45] D.W. Davidson, R.H. Cole, Dielectric relaxation in glycerol, propylene glycol, and nPropanol, J. Chem. Phys. 19 (1951) 1484–1490.

[46] R. Andoulsi-Fezei, N. Sdiri, K. Horchani-Naifer, M. Ferid, Effect of temperature on the electrical properties of lanthanum ferrite, Spectrochim. Acta Mol. Biomol. Spectrosc. 205 (2018) 214–220.

[47] W. Wang, W. Sun, G. Zhang, Y. Wang, Z.X. Cheng, Magnetic domain-wall induced ferroelectric polarization in rare-earth orthoferrites $AFeO_3$ (A = Lu, Y, Gd): first-principles calculations, J. Mater. Chem. C. 7 (2019) 10059–10065.

[48] V.V. Triguk, I.I. Makoed, A.F. Ravinski, Electronic structure and improper electric polarization of samarium orthoferrite, Phys. Solid State 58 (2016) 2443–2448.

[49] H.J. Zhao, L. Bellaiche, X.M. Chen, J. Íñiguez, Improper electric polarization in simple perovskite oxides with two magnetic sublattices, Nat. Commun. 8 (2017) 14025.

[50] C.G. Koops, On the dispersion of resistivity and dielectric constant of some semiconductors at audiofrequencies, Phys. Rev. 83 (1951) 121–124.

[51] M.K. Warshi, V. Mishra, A. Sagdeo, V. Mishra, R. Kumar, P.R. Sagdeo, Synthesis and characterization of $RFeO_3$: experimental results and theoretical prediction, Adv. Mater. Process. Techn. 4 (2018) 558–572.

[52] G.M. Tsangaris, G.C. Psarras, G.M. Tsangaris, Electric modulus and interfacial polarization in composite polymeric systems, J. Mater. Sci. 33 (1998) 2027–2037.

[53] X.Y. Zhao, X.L. Wang, H. Lin, Z.Q. Wang, Electronic polarizability and optical basicity of lanthanide oxides, Phys. B. 392 (2007) 132–136.

[54] X.L. Wang, D.W. Yu, X. Han, X.Y. Zhao, Study on lanthanide oxides materials in material engineering with a new method, Adv. Mater. Res. 568 (2012) 340–343.